A&A 451, 917–924 (2006)
DOI: 10.1051/0004-6361:20053845

Astronomy & Astrophysics

[CII] 158 μm emission and metallicity in photon dominated regions⋆

M. Röllig[1], V. Ossenkopf[1,2], S. Jeyakumar, J. Stutzki[1], and A. Sternberg[3]

[1] I. Physikalisches Institut, Universität zu Köln, Zülpicher Str. 77, 50937 Köln, Germany
e-mail: roellig@ph1.uni-koeln.de
[2] SRON National Institute for Space Research, PO Box 800, 9700 AV Groningen, The Netherlands
[3] School of Physics and Astronomy, Tel Aviv University, Ramat Aviv 69978, Israel

Received 18 July 2005 / Accepted 14 November 2005

ABSTRACT

We study the effects of a metallicity variation on the thermal balance and [CII] fine-structure line strengths in interstellar photon dominated regions (PDRs). We find that a reduction in the dust-to-gas ratio and the abundance of heavy elements in the gas phase changes the heat balance of the gas in PDRs. The surface temperature of PDRs decreases as the metallicity decreases except for high density ($n > 10^6$ cm^{-3}) clouds exposed to weak ($\chi < 100$) FUV fields where vibrational H_2-deexcitation heating dominates over photoelectric heating of the gas. We incorporate the metallicity dependence in our KOSMA-τ PDR model to study the metallicity dependence of [CII]/CO line ratios in low metallicity galaxies. We find that the main trend in the variation of the observed CII/CO ratio with metallicity is well reproduced by a single spherical clump, and does not necessarily require an ensemble of clumps as in the semi-analytical model presented by Bolatto et al. (1999).

Key words. ISM: abundances – ISM: structure – ISM: clouds – ISM: general – galaxies: ISM – galaxies: abundances

1. Introduction

The bright line emission from photon-dominated regions (PDRs) is one of the key tracers of the star formation activity throughout the evolution of galaxies in the course of the cosmological evolution. Hence, proper modeling of PDR emission is of central importance for the interpretation of the observations, in order to derive the physical parameters and the chemical state of the ISM in external galaxies. The extensive literature on PDR emission, both observationally and from the modeling side, has largely concentrated on bright Galactic sources and starburst galaxies. The effect of different metallicity for the resulting PDR emission has, up to now, drawn little attention. It is, however, very important in order to cover the full course of galactic evolution, starting with low metallicity material of cosmological origin. Many nearby galaxies, such as dwarf galaxies, irregular galaxies and the Magellanic Clouds have a low metallicity (Lisenfeld & Ferrara 1998; Kunth & Östlin 2000; Pustilnik et al. 2002; Lee et al. 2003). Within the Galaxy, as well as in other spiral galaxies, there is a radial decrease in the metallicity of molecular clouds and associated HII regions (Zaritsky et al. 1994; Arimoto 1996; Giveon et al. 2002; Bresolin et al. 2004). These systems provide the opportunity to study star formation and photon-dominated regions (PDRs) for a variety of metallicities.

In PDRs the molecular gas is heated by the far-ultraviolet (FUV) radiation field, either the strong FUV radiation in the vicinity of hot young stars, or weak average FUV fields in the Galaxy. The gas cools through the spectral line radiation of atomic and molecular species (Hollenbach & Tielens 1999; Sternberg 2004). The gas-phase chemistry together with a depth dependent FUV intensity lead to the formation of atomic and molecular species at different depths through the cloud. This typical stratification of PDRs is for example reflected by the the H/H_2 and C^+/C/CO transitions (Sternberg & Dalgarno 1995; Boger & Sternberg 2005). At low visual extinctions the gas is cooled by emission of atomic fine-structure lines, mainly [CII] 158 μm and [OI] 63 μm. At larger depths, millimeter, sub-millimeter and far-infrared molecular rotational-line cooling (CO, OH, H_2O) becomes important together with the interaction of dust and gas. Physical conditions such as temperature and density can be derived, by comparing the observed line emissions with model predictions (Le Bourlot et al. 1993; Wolfire et al. 1995; Störzer et al. 1996; Warin et al. 1996; Kaufman et al. 1999; Zielinsky et al. 2000; Störzer et al. 2000; Gorti & Hollenbach 2002).

[CII] emission is a widely used diagnostic indicator of star formation (Stacey et al. 1991; Pierini et al. 1999; Malhotra et al. 2000; Boselli et al. 2002b; Pierini et al. 2003; Kramer et al. 2004). Observations suggest that low metallicity systems have higher [CII] to CO rotational line ratios compared to the Galactic value. In particular, the intensity ratio $I_{[CII]}/I_{CO}$ may vary from ∼1000 in the inner Milky Way, up to $\sim 10^5$ in extremely low metallicity systems (e.g. Madden et al. 1997; Mochizuki et al. 1998; Bolatto et al. 1999; Madden 2000; Hunter et al. 2001). Several studies have suggested that a lower abundance of heavy elements affects the chemical structure of PDRs and the cooling line emission, and that estimates of molecular gas masses from the observed CO($J = 1-0$) line intensities using the standard conversion factor may underestimate the true masses in such objects (Wilson 1995; Israel 1997; Israel et al. 2003; Rubio et al. 2004).

Bolatto et al. (1999) modelled the metallicity variation of the line ratio [CII]/CO(1–0), for an ensemble of spherical "clumps", assuming an inverse relation between the size of the C^+ region

⋆ Appendices are only available in electronic form at
http://www.edpsciences.org

and the metallicity. However the sizes of the C^+, C and CO regions also depend on the chemistry in PDRs and the chemical network is modified at low metallicities (Lequeux et al. 1994). Additionally it has been suggested that the size of the C^+, C and CO regions may also significantly depend on the overall cloud morphology, e.g. density variations (Hegmann & Kegel 2003) and velocity fluctuations (Röllig et al. 2002). Moreover the temperature of the molecular gas might depend on the metallicity which affects the observable line intensities (Wolfire et al. 1995).

We study the effects of metallicity changes on the temperature and chemical structure of PDRs. In Sect. 2 we consider the dependence of the PDR gas temperature on the metallicity using a simplified semi-analytic model and compare it with numerical results from full PDR model calculations. Our computations were carried out using an updated version of our spherical KOSMA-τ model (Störzer et al. 1996) which was originally adapted from the plane-parallel model presented by Sternberg & Dalgarno (1995). In Sect. 3 we examine the predicted size of the C^+ zones as a function of metallicity. We then model the strength of the [CII] emission and investigate the dependence of the [CII]/CO($J = 1-0$) line ratio on the metallicity. Finally we compare the results with observational data in Sect. 4.

2. Metallicity dependence of the surface temperature

The basic cooling and heating processes in PDRs, are affected by the abundances of elements as well as the content and the composition of dust grains (Wolfire et al. 1995; Kaufman et al. 1999). The dust-to-gas ratio (D/G) and the optical properties of the dust may depend on the metallicity, Z. Fits to observations suggest that the ratio depends almost linearly on the metallicity, $D/G \propto Z^{1.146}$ (Boselli et al. 2002a). There are other studies that find deviations from linearity for higher values of D/G (Lisenfeld & Ferrara 1998). Li & Draine (2002) suggested that the mixture of PAHs in the metal-poor SMC differs from the Milky Way. There are a few observations indicating that PAHs could have been destroyed by intense UV fields at low metallicities (Thuan et al. 1999; Bolatto et al. 2000), but the detailed composition of dust in low metallicity environments and the influence on its optical properties is not yet understood. Because of the insufficient knowledge we assume in our model that the composition of the grains does not change with metallicity and that the dust-to-gas ratio and the gas-phase abundance of heavy elements scale linearly with Z.

Changes in Z affect the abundances of major coolants as well as the electron densities in PDRs. Additionally, a reduction in the dust abundance diminishes the UV opacity, the photo electric heating rate, and the H_2 formation rate. These changes affect the temperature and chemistry in the surface layers where C^+ is most abundant.

The dependence of the surface gas temperature on Z can be estimated considering the balance of cooling and heating. The dominant cooling processes depend predominantly on the total hydrogen gas density n. [OI]63 μm, [CII]158 μm emission, and gas-grain collisions are important cooling processes (Burke & Hollenbach 1983; Störzer et al. 1996). Their relative importance in the different regimes is discussed in Sect. 2.2.1. The dominant heating process depends on the far-ultraviolet (FUV; 6−13.6 eV) field and the density. Grain photo-electric emission (PE) (d'Hendecourt & Léger 1987; Lepp & Dalgarno 1988; Verstrate et al. 1990; Bakes & Tielens 1994), collision deexcitation of FUV pumped molecular hydrogen $H_2^\star$ (Sternberg & Dalgarno 1989; Burton et al. 1990) and heating from H_2 formation play important roles. They are discussed in detail in Sect. 2.2.2. By explicitly considering the metallicity dependence of each of these cooling and heating processes and identifying the dominant processes in the different parameter regimes we will show how the energy balance in PDRs depends on Z for a quantitative understanding of the PDR surface temperature.

2.1. The KOSMA-τ PDR model

In our study we use an updated version of the spherical PDR code described in detail by Störzer et al. (1996). Briefly, this model solves the coupled equations of energy balance (heating and cooling), chemical equilibrium, and radiative transfer in spherical geometry. The PDR-clumps are characterized by a) the incident FUV field intensity χ, given in units of the mean interstellar radiation field of Draine (1978); b) the clump mass; and c) the average density of the clump, for a radial power-law density distribution with index γ. We incorporate the effects of varying metallicity by varying the assumed abundance of dust grains and heavy elements. The following parameters are multiplied by the metallicity factor Z: (a) the total effective FUV dust absorption cross section per hydrogen nucleus σ; (b) the photoelectric heating rate; (c) the H_2 formation rate; (d) the metal abundance. We consider a range of Z from 0.2 to 1. For $Z = 1$ we use $\sigma = 1.9\times10^{-21}$ cm^2, C/H = 1.4×10^{-4}, and O/H = 3×10^{-4} as standard values for the local ISM (Hollenbach & Tielens 1999). These values are slightly lower than recent solar values of $12 + \log(\mathrm{O/H}) \approx 8.7$ by Asplund et al. (2004). For a detailed discussion see Baumgartner & Mushotzky (2005). We do not consider gas depletion on grains.

2.2. Semi-analytic approximations

The results of the full numerical computations can be understood and anticipated using some simplifying semi-analytical approximations. Here, we focus on the surface temperature of the PDR at $A_V = 0$, as we are not interested in the shielding properties of low-metal PDRs but in the thermal behavior of the low-extinction region dominating the CII emission. We study how the thermal properties respond to altered elemental abundance. We assume the molecular cloud is sufficiently thick such that it absorbs all radiation coming from the backside, leading to an emission line escape probability $\beta(\tau = 0) = 1/2$ at the surface.

2.2.1. Cooling

In the simplified model we include the three main cooling processes: [CII] and [OI] line cooling and gas-grain collisional cooling (Burke & Hollenbach 1983; Störzer et al. 1996). Gas cooling is generally dominated by fine structure emission of [CII] and [OI]. Gas-grain cooling starts to contribute significantly for high densities. At $n \gtrsim 10^6$ cm^{-3} the coupling between gas and dust is strong enough so that the efficient cooling of the dust by infrared radiation also provides a major coolant to the gas. The total cooling rate per unit volume by these radiative processes is the sum

$$\Lambda_{\mathrm{tot}} = \Lambda_{\mathrm{CII}} + \Lambda_{\mathrm{OI}} + \Lambda_{\mathrm{g-g}}. \quad (1)$$

With the abundance of carbon, oxygen, and dust scaling with the metallicity, the total cooling rate is also linear in Z.

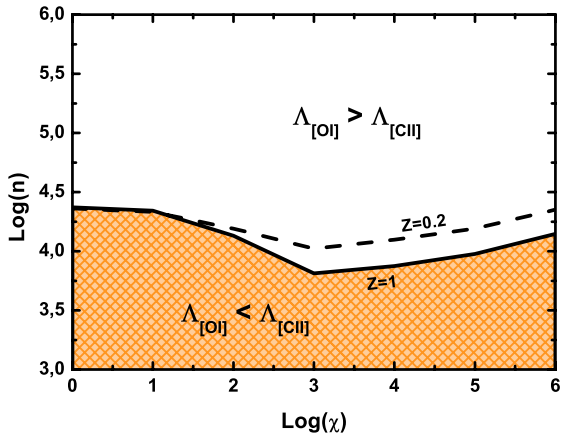

Fig. 1. The solid and dashed line represent the points in $n - \chi$-parameter space where $\Lambda_{\rm OI} = \Lambda_{\rm CII}$ for metallicities of $Z = 1$ and $Z = 0.2$ respectively.

Analytic expressions for the three cooling processes are derived in Appendix A. In Fig. 1 we show the relation between the fine-structure line cooling contributions as a function of n and χ for two different values of Z. The region in parameter space where [CII] cooling dominates over [OI] is shaded in gray. For densities above $10^{4.5}$ cm^{-3} [CII] cooling is quenched and [OI] cooling dominates. At all lower densities [CII] cooling dominates. Every point in Fig. 1 corresponds to a different equilibrium temperature and resulting ratio $\Lambda_{\rm CII}/\Lambda_{\rm OI}$. The dependence on χ in Fig. 1 results from the implicit temperature dependence of the fine-structure cooling rates. Grain cooling dominates only for densities greater than 10^6 cm^{-3}.

2.2.2. Heating

The dominant heating process depends on the FUV field intensity and density. For high intensities grain photo-electric heating dominates. The rate for this process, given by Bakes & Tielens (1994), is $\Gamma_{\rm PE} = 10^{-24} \epsilon\, G_0 n_{\rm H}\, Z$ erg s^{-1} cm^{-3} where ϵ is the photoelectric heating efficiency and G_0 is the UV intensity in units of the Habing field. Following Bakes & Tielens (1994) the photoelectric heating efficiency is given by:

$$\epsilon = \frac{3 \times 10^{-2}}{1 + 2 \times 10^{-4} (G_0 T^{1/2}/n_{\rm e})} \tag{2}$$

with $n_{\rm e}$ being the electron density in cm^{-3} and T the dust temperature in K. We set $G_0 = 1.71 \times 0.5\, \chi$ to account for the relative factor of 1.71 between the Habing and Draine fields, and the fact that at the surface of optically thick clouds radiation is incident from a solid angle of $2\,\pi$ rather than $4\,\pi$ steradians. In evaluating the efficiency ϵ we use the analytic expression for the electron density derived in Appendix B:

$$n_{\rm e} \approx 0.84 \times 10^{-4}\, n Z \left(1 + \sqrt{1 + 14.4\, \frac{T^{0.75}}{n Z^2}}\right) \text{ cm}^{-3}. \tag{3}$$

It is common to express the *net* PE heating rate as $\Gamma_{\rm PE}^{\rm net} = \Gamma_{\rm PE} - \Lambda_{\rm rec}$, where $\Lambda_{\rm rec}$ is the cooling rate due to electron recombination. We adopt the analytical fit from Bakes & Tielens (1994):

$$\Lambda_{\rm rec} = 3.49 \times 10^{-30}\, T^{0.944} \left(\frac{G_0\, T^{1/2}}{n_{\rm e}}\right)^{\frac{0.735}{T^{0.068}}} n_{\rm e}\, n\, Z. \tag{4}$$

In dense PDRs a second important heating source is the collisional deexcitation of vibrationally excited $H_2^\star$. The rate for this process can be expressed as

$$\Gamma_{H_2^\star} = \chi\, P\, n_{H_2}\, \Delta E\, f \quad \text{erg s}^{-1}\text{cm}^{-3}, \tag{5}$$

with n_{H_2} is the density of molecular hydrogen, $P = 2.9 \times 10^{-10}$ s^{-1} is the pumping rate for a unit FUV field, $\Delta E \approx 23\,500$ K is the characteristic vibrational transition energy, and an efficiency factor f accounting for all processes that may reduce the number of de-exciting collisions (see Appendix B). The balance equation for the formation and destruction of H_2 is

$$n\, n_{\rm H}\, R = \chi\, D\, n_{H_2} \tag{6}$$

where $D = 2.6 \times 10^{-11}$ s^{-1} is the total dissociation rate in a $\chi = 1$ FUV field, and $R = R_0\, Z$ is the grain surface H_2 formation rate coefficient (cm^3 s^{-1}). Here, it is implicitly assumed that dust grains are always covered by enough H atoms, so that the recombination rate is only limited by the number of H-dust collisions. We use the standard recombination rate R_0 by Hollenbach & Salpeter (1971); Hollenbach et al. (1971):

$$R_0 = 3 \times 10^{-18}\, f_{\rm a}\, S\, T^{1/2} \text{ cm}^3 \text{ s}^{-1}, \tag{7}$$

where the accommodation coefficient, $f_{\rm a}$ and the sticking probability S are independent of Z (Hollenbach & McKee 1979). Cazaux & Spaans (2004) show that gas-phase formation of H_2 becomes important for $Z < 10^{-3}$, well below the minimum value of Z we consider here.

The density of atomic and molecular hydrogen is determined by Eq. (6) and can be written as

$$n_{\rm H} = n \frac{1}{1 + 2\,\alpha} \quad \text{and} \quad n_{H_2} = n \frac{\alpha}{1 + 2\,\alpha} \tag{8}$$

respectively, with $\alpha = n\, R/(\chi\, D)$ being the ratio between formation and destruction rate coefficients. For example, for $\chi = 1$ and $n = 10^3$ cm^{-3} more than 99% of the gas at the surface is atomic. For $Z = 1$ and a unit Draine field, $\alpha = 1$ and $n_{\rm H} = n_{H_2}$, for densities $n \approx 10^6$ cm^{-3}. As only R depends on Z, it follows that $\alpha \propto Z$ and the density n at which the H and H_2 densities are equal at the cloud surface scales as $1/Z$.

From Eqs. (5)–(7) it follows that

$$\Gamma_{H_2^\star} = \left(\frac{P}{D}\right) R_0\, Z\, n\, n_{\rm H}\, \Delta E\, f \quad \text{erg s}^{-1}\,\text{cm}^{-3}. \tag{9}$$

We see that $\Gamma_{H_2^\star}$ is maximized when $n_{\rm H} = n$ and all of the hydrogen is atomic. The efficiency factor f in Eq. (5) is largest in the limit of high gas density and low FUV intensity, where radiative processes become negligible in depopulating the excited vibrational levels compared to collisional deexcitation. For a temperature of $T = 100$ K, $Z = 1$, $\chi = 1$, and $n = 10^3$ cm^{-3} we obtain $\Gamma_{H_2^\star}^{\rm max} \approx 1.8 \times 10^{-24}$ erg cm^{-3} s^{-1} with $f = 2.8 \times 10^{-3}$.

This is in good agreement with the results from the numerical PDR model shown in Fig. C.1 in Appendix C. The assumption of a constant formation rate R_0 is valid for $\chi \lesssim 10^3$. A higher UV field the dust temperature increases leading to a rapid reduction of the accommodation coefficient $f_{\rm a}$. Hence in our calculations the maximum H_2 heating rate drops for $\chi \gtrsim 10^3$ as shown in the bottom plot in Fig. C.1 in Appendix C.

H_2 not only contributes to the heating, but cools the gas at higher temperatures (Sternberg & Dalgarno 1989). To account for the cooling we define the net heating rate $\Gamma_{H_2}^{\rm net} = \Gamma_{H_2^\star} - \Lambda_{H_2}$.

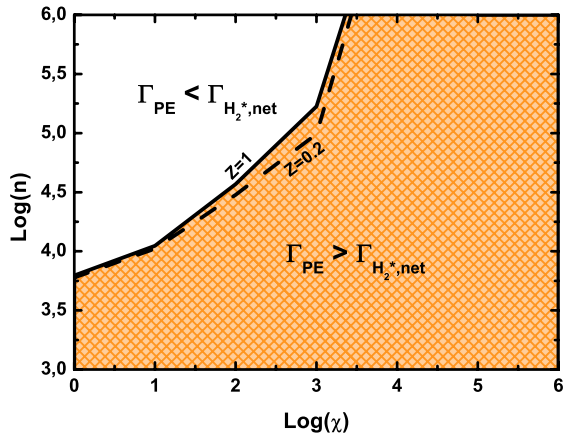

Fig. 2. The solid and dashed line represent the points in $n-\chi$-parameter space where $\Gamma_{H_2^*,\rm net} = \Gamma_{\rm PE}$ for metallicities of $Z = 1$ and $Z = 0.2$ respectively.

Using the analytic approximations to the molecular level structure of H_2 derived in Appendix C we obtain

$$\begin{aligned}\Gamma_{H_2^\star} &= n_{H_2}\frac{\chi P}{1+\left(\frac{A_{\rm eff}+D_{\rm eff}}{\gamma n}\right)}\Delta E \\ &= n_{H_2}\frac{9.4\times10^{22}\chi}{1+\left(\frac{1.9\times10^{-6}+4.7\times10^{-10}\chi}{\gamma n}\right)} \qquad (10)\\ \Lambda_{H_2} &= n\,n_{H_2}\,\Delta E\,\gamma\,\exp(-\Delta E/kT)\\ &\quad\times\frac{A+D}{\gamma n+A+D}\\ &= n\,n_{H_2}\,9.1\times10^{-13}\,\gamma\,\exp\left(-6592\,{\rm K}/T\right)\\ &\quad\times\frac{8.6\times10^{-7}+2.6\times10^{-11}\chi}{\gamma n+8.6\times10^{-7}+2.6\times10^{-11}\chi} \qquad (11)\end{aligned}$$

with a collisional rate coefficient $\gamma = 5.4\times10^{-13}\,\sqrt{T}$ s^{-1} cm^{-3}. As the molecular constants do not depend on the metallicity, only the Z-dependence of n_{H_2} changes the H_2 de-excitation heating.

The relative reduction of the H_2 heating at high radiation fields is demonstrated in Fig. 2 comparing the PE heating and the H_2 de-excitation heating for the different parameter regimes. We see that at any given density $\Gamma_{\rm PE}^{\rm net}$ exceeds $\Gamma_{H_2}^{\rm net}$ beyond a certain χ value, but that this limit increases with the gas density.

Although $\Gamma_{\rm PE}$ and $\Gamma_{H_2^\star}$ are the two main heating terms it is necessary to account for a third process in order to achieve a reasonable approximation of the full energy balance. For UV fields $\chi < 10^3$, and densities $n < 10^4$ cm^{-3}, H_2 formation heating may contribute significantly. Assuming that each formation process releases 1/3 of its binding energy to heat the gas (Sternberg & Dalgarno 1989), the corresponding heating rate is:

$$\Gamma_{\rm form} = 2.4\times10^{-12}\,R\,n\,n_{\rm H}\ \ {\rm erg\,cm^{-3}\,s^{-1}}. \qquad (12)$$

Summing over all three processes we obtain the total heating rate

$$\Gamma_{\rm tot} = \Gamma_{\rm PE}^{\rm net} + \Gamma_{H_2}^{\rm net} + \Gamma_{\rm form}. \qquad (13)$$

2.2.3. Metallicity dependence

An inspection of the heating and cooling functions described above reveals their metallicity dependence. Table 1 summarizes the scaling relations. The radiative cooling functions are linear in Z. The photoelectric heating depends on the metallicity via $\epsilon(Z)\times Z$. The influence of $\epsilon(Z)$ can be neglected as long as $n/\chi \gtrsim 100$. Thus, for low UV fields $\Gamma_{\rm PE} \sim Z$. For higher values of χ the efficiency accounts for an additional influence due to the electron density which is proportional to Z for high densities, and independent of Z for very low densities. The metallicity dependence for densities between $10^3...10^5$ cm^{-3} is not trivial. Equation (3) shows that the electron density is linear in Z for very high n. In the intermediate range this dependence roughly shifts from Z^0 to Z^1. This leads to $\Gamma_{\rm PE} \sim Z^2$ for high values of n and $\Gamma_{\rm PE} \sim Z$ for very low densities.

Table 1. Metallicity dependence of the individual heating processes.

	Low UV field $\chi < 100$	High UV field $\chi \gg 100$
high density ($n \gtrsim 10^6$)	$\Gamma_{\rm PE} \sim Z$ $\Gamma_{H_2^*} \sim \frac{Z}{1+2Z}$ $\Gamma_{H_2-{\rm form}} \sim Z$ $\Lambda_{\rm rec} \sim Z^{1.5}$ $\Lambda_{\rm tot} \sim Z$	$\Gamma_{\rm PE} \sim Z^2$ $\Gamma_{H_2^*} \sim Z$ $\Gamma_{H_2-{\rm form}} \sim Z$ $\Lambda_{\rm rec} \sim Z^{1.5}$ $\Lambda_{\rm tot} \sim Z$
low density ($n \lesssim 10^3$)	$\Gamma_{\rm PE} \sim Z$ $\Gamma_{H_2^*} \sim Z$ $\Gamma_{H_2-{\rm form}} \sim Z$ $\Lambda_{\rm rec} \sim Z$ $\Lambda_{\rm tot} \sim Z$	$\Gamma_{\rm PE} \sim Z...Z^{1.5}$ $\Gamma_{H_2^*} \sim Z$ $\Gamma_{H_2-{\rm form}} \sim Z$ $\Lambda_{\rm rec} \sim Z...Z^{1.5}$ $\Lambda_{\rm tot} \sim Z$

The recombination cooling depends on the metallicity through the electron density, resulting in $\Lambda_{\rm rec} \sim Z$ and $Z^{1.5}$ for low and high densities respectively. The Z-dependence in the hydrogen heating (Eqs. (10) and (11)) comes from the hydrogen density which depends on the metallicity as $Z/(1+2Z)$ for high densities and low values of χ, and as Z otherwise.

As a result we show in Fig. 3 the surface temperature of model clouds for a variety of different UV field strengths and densities computed from the analytic approximation and from the full KOSMA-τ PDR model. We covered a parameter space ranging from $n = 10^3\ldots10^6$ cm^{-3} and $\chi = 10^0\ldots10^6$. It is obvious that the metallicity dependence varies strongly over the parameter space. We obtain a good agreement for low and high UV fields. Even in the intermediate UV and density range, where the quantitative accord is weaker, the qualitative dependence of $T_{\rm surf}$ on Z is well reproduced by the semi-analytical model.

The Z-dependence of the temperature can be understood by comparing the dominant net rates of heating Γ/Z and cooling Λ/Z. At high UV fields, where the PE heating dominates, the heating is proportional to Z^2 at high densities. For a density of $n = 10^3$ the PE heating is $\sim Z\,\sqrt{Z^2+1}$. Due to the high UV field $n/\chi < 100$ for all given densities thus the electron density influences the heating also for small values of n. If the density increases the term $14.4\,T^{0.75}/n$ vanishes and $\Gamma_{\rm PE} \sim Z^2$. This is reflected in the slopes of the surface temperature in Fig. 3(top). For intermediate FUV fields we find a similar behavior with the addition that n/χ is <100 for high densities and ≥100 for low densities, thus the metallicity dependence shifts from Z^2 to Z with increasing density. This shift can be seen in the middle plot in Fig. 3.

When H_2 vibrational de-excitation heating dominates (compare Fig. 2), the corresponding rate varies as $Z/(1+2Z)$, hence the surface temperature drops as $1/(1+2Z)$. This is shown for $n = 10^6$ cm^{-3} in Fig. 3(middle) and for $n \geq 10^4$ cm^{-3} in the bottom panel of Fig. 3 which gives the temperatures for a FUV field strength of $\chi = 1$. For low FUV fields and low densities the temperature is proportional to Z due to the PE heating as seen in Fig. 3(bottom).

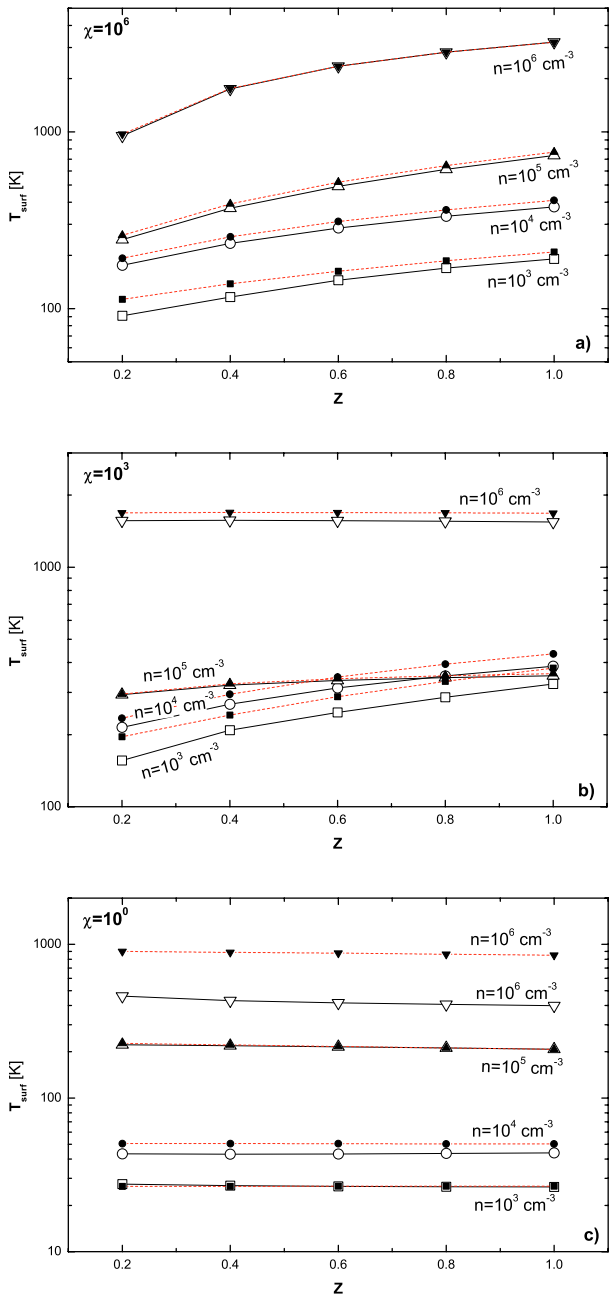

Fig. 3. Comparison of the KOSMA-τ results (open symbols) and the semi-analytic values (filled symbols) for the surface temperature against the metallicity. The *top panel* **a)** is for an UV field of $\chi = 10^6$, the *bottom plot* **b)** is for $\chi = 10^3$, and the *bottom panel* **c)** is for an UV field strength of $\chi = 1$. The different symbols indicate different surface densities.

The offset between the semi-analytical approximation and numerical result for $\chi = 10^3$ is due to a small contribution of additional cooling processes in that parameter range. This increases the total cooling efficiency and hence the temperatures in the full numerical calculations are smaller. This also holds for $n = 10^6$ cm^{-3} and $\chi = 1$. In that case the cooling is dominated by CO line cooling which is stronger than [OI] 63 μm and also by H_2O cooling which is comparable to [OI] 63 μm. Here our initial assumptions are clearly underestimating the overall cooling. Even so this does not change the behavior with Z which is well reproduced.

As there is some debate on D/G we tested as an extreme example $D/G \propto Z^2$ instead of linearity. This mainly changes the behavior of the heating rates. The dominant surface cooling processes do not depend on D/G, but only on the elemental abundances, while the heating processes are affected by an altered D/G. This leads to a decreased heating efficiency for $Z < 1$, hence the surface temperature is significantly lower if we assume $D/G \propto Z^2$. In the extreme example of $\chi = 10^6$, $n = 10^6$ cm^{-3}, and $Z = 0.2$ we find $T_{\rm surf} = 240$ K, a factor of 4 smaller than for $D/G \propto Z$. The cooling inside the cloud also depends somewhat on D/G, since the escape probability of cooling lines depends on the dust attenuation.

3. Variation of the C^+ layer size with metallicity

At the surface of the PDR the FUV radiation ionizes almost all of the carbon atoms. At larger depths the FUV intensity decreases and carbon recombines and is eventually incorporated into CO molecules. Thus, a PDR clump can be subdivided into a CO core surrounded by an atomic carbon shell and an outer C^+ envelope. We examine here, the thickness of the C^+ envelope as a function of metallicity Z. We define the C^+ envelope thickness as the distance from the cloud surface to the depth where the abundances of C and C^+ are equal.

The dominant reaction channels for the formation and destruction of C^+ are

$$C + \nu \rightarrow C^+ + e^-,$$

$$C^+ + e^- \rightarrow C + \nu$$

and

$$C^+ + H_2 \rightarrow CH_2^+ + \nu.$$

Assuming, that these are the only reactions which influence the C^+ abundance, the balance equation for the abundance of C^+ can be written as,

$$\chi\, I\, n_{\rm C} = a_{\rm C}\, n_{\rm C^+}\, n_{\rm e} + k_{\rm C}\, n_{\rm C^+}\, n_{\rm H_2} \qquad (14)$$

where I is the photoionization rate, $a_{\rm C}$ and $k_{\rm C}$ are the recombination and radiative association rate coefficients. We assume that the photoionization rate is attenuated exponentially as $\exp(-p\, A_{\rm V})$ where the factor $p = 3.02$ accounts for the difference in the opacity between visual and FUV wavelengths. As $A_{\rm V}$ is determined by dust extinction it scales linearly with Z. In the KOSMA-τ model we account for an isotropic FUV field, and integrate over 4π ray angles. The ionization rate is then given by,

$$I = 3 \times 10^{-10} \chi \int_1^\infty \frac{\exp(-3.02\, A_{\rm V}\, \mu)}{\mu^2} {\rm d}\mu. \qquad (15)$$

The integral is the second order exponential integral $E_2(3.02\, A_{\rm V})$ where $\mu = \cos\Theta$ and Θ is the angle between the ray and the normal direction.

We have defined the radial point $r_{\rm C^+}$ as the location where the abundances of C^+ and C are equal, $n_{\rm C^+} = n_{\rm C}$. If we neglect the contribution of CO at $r_{\rm C^+}$ then $n_{\rm C^+} = X_{\rm C}\, n/2$ there. Results from the PDR model suggest, that the electron density, $n_{\rm e}(Z) \approx 2\, n_{\rm C^+}(Z)$, thus $n_{\rm e}(Z) \approx \hat{n}_{\rm C}(Z = 1)\, Z$. For the sake of simplicity we chose this expression for $n_{\rm e}$ rather than the one introduced in Eq. (3) which would introduce an additional temperature dependence. With $X_{\rm C} = 1.4 \times 10^{-4}\, Z$ and molecular

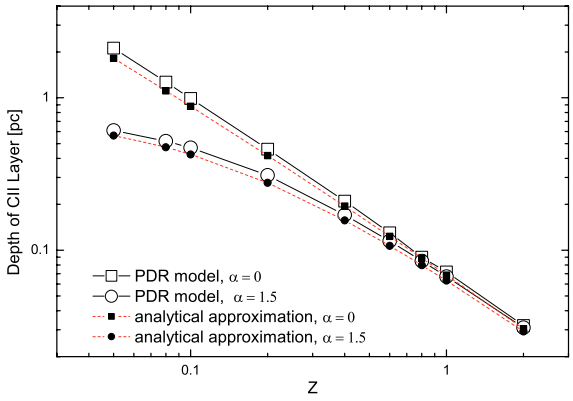

Fig. 4. The width of the C^+ layer is plotted against the metallicity. The open circles represent spherical clump of mass $M = 10^3\ M_\odot$, density $n_0 = 10^4$ cm^{-3}, FUV field $\chi = 100$, and the power-law index of the density profile, $\gamma = 1.5$, whereas the open squares represent a spherical clump of mass of $10^6\ M_\odot$ with $\gamma = 0$. The filled circles and squares represent our analytical estimates as explained in Sect. 3.

hydrogen dominating the gas density, $n_{H_2} = n/2$, we can resolve Eq. (14) for the density at r_{C^+}

$$n(r_{C^+}) = \frac{3 \times 10^{-10}\,\chi\,E_2\,(3.02\,A_V(r_{C^+}))}{a_C\,Z\,1.4 \times 10^{-4} + 0.5\,k_C}. \quad (16)$$

For a given radial density distribution $n(r)$ and FUV field χ, Eq. (16) can be numerically solved to obtain r_{C^+}, or correspondingly the width of the C^+ layer $D_{C^+} = R - r_{C^+}$. In Fig. 4 we compare the results from this equation with detailed PDR model calculations using the KOSMA-τ model for $n_0 = 10^4$ cm^{-3} and $\chi = 100$. Here two types of density structures are used: (a) $n(r) = n_0\,(r/R)^{-\gamma}$ for $0.2\,R \le r < R$, $n(r) = 0$ for $r > R$, and $n = n_0\,0.2^{-\gamma}$ for $r < 0.2R$, with the total cloud radius R; (b) a constant density, $n(r) = n_0$, or equivalently $\gamma = 0$.

The squares representing the constant density model show that the C^+ layer width depends approximately as $Z^{-1.1}$ on the metallicity which closely matches with the assumption of an inverse proportionality by Bolatto et al. (1999). The circles in Fig. 4 represent the model by the $\gamma = 1.5$. They can be numerically fitted with function, $D_{C^+} = (1.195 + 5.758Z)^{-1.47}$ pc. Figure 4 shows that our results using Eq. (16) agrees well with the model calculations. However the estimated widths are slightly higher than the model calculations, which reflects the fact that there are more reactions which quantitatively influence the chemistry of C^+.

4. [CII] emission as a function of *Z*

The [CII] emission as well as the [CII]/CO(1−0) line ratio is typically considered to be a good tracer of star formation (Stacey et al. 1991). The intensity ratio $I_{[CII]158\,\mu m}/I_{CO(1-0)}$, observed in many nearby low metal galaxies, is higher than for sources with solar and super-solar metallicities (Madden et al. 1997; Mochizuki et al. 1998; Bolatto et al. 1999; Madden 2000; Hunter et al. 2001). Table 2 summarizes available line ratios and metallicities of nearby galaxies. The corresponding numbers for Orion are also given as a Galactic reference.

This dependence has been modelled by Bolatto et al. (1999) assuming that the size of the C^+ region scales inversely with metallicity, and assuming a constant temperature for the gas.

Table 2. Metallicities and observed [CII]/CO(1−0) line ratios of nearby galaxies and Galactic star forming regions.

Object	12 + log (O/H)	[CII]/CO(1−0)	References
NGC 1068	9.07	6000	14, 2, 12
NGC 1156	8.39	10 000	4
NGC 1313	8.25	11 740	14, 7
NGC 1569	8.08	37 000	13, 4, 6
NGC 4449	8.3	14 000	8, 6
NGC 4736	9	2500	14, 2, 12, 10
NGC 6946	9	900	14, 12
IC 10	8.19	14 000	14, 8, 6
IZw 36	7.93	<3000	8
M83	9.16	8000	14, 2, 5
M51	9.23	3500	14, 9, 5
IC 4622	8.09	34 000	3, 4
Orion	8.75	6000	2, 11
LMC	8.35	5600	1
30 Doradus	8.43	69 000	1
SMC	8.03	13 000	1

References. (1) Bolatto et al. (1999); (2) Crawford et al. (1985); (3) Heydari-Malayeri et al. (1990); (4) Hunter et al. (2001); (5) Kramer et al. (2005); (6) Lord et al. (1995); (7) Luhmann et al. (2003); (8) Mochizuki et al. (1998); (9) Nikola et al. (2001); (10) Petitpas & Wilson (2003); (11) Simon et al. (1997); (12) Stacey et al. (1991); (13) Talent (1980); (14) Zaritsky et al. (1994).

For our spherical PDR model we compute the surface brightness as function of clump mass/radius and metallicity. The surface brightness is the projected average intensity

$$\bar{I} = \frac{2\,\pi\,\int_0^R I(p)p\,\mathrm{d}p}{\pi\,R^2} \quad (17)$$

of the spherical clump, where $I(p)$ is the specific intensity along a ray with impact parameter p (Störzer et al. 1996). The line intensities depend on the thermal and chemical structure of the cloud. Additionally, for spherical clouds an effective area-filling factor of the emissive region has to be considered. Particularly lines, which are formed in central regions of the cloud are influenced by this area-filling factor. A good example is the surface brightness of ^{12}CO(1−0). For a density of $n = 10^3$ cm^{-3} and low metallicities almost the whole cloud is devoid of CO due to photodissociation. A higher density or metallicity results in a larger CO core and a higher surface brightness. For species which are mainly emitting at the surface of the cloud this filling effect is negligible.

In the prior sections we derived approximate expressions for the surface temperature of a PDR as well as for the expected depth of the C^+ envelope. We can use these approximations to estimate the total [CII] surface brightness of the PDR. The local emissivity $\Lambda_{[CII]}(r)$ from Eq. (A.2) can be used to calculate the line integrated intensity of the PDR in the optically thin case

$$I_{int} = \int_{r_{C^+}}^{R} 4\,\pi\,r^2\,\frac{\Lambda_{[CII]}(r)}{4\,\pi}\mathrm{d}r \ \ \mathrm{erg\,s^{-1}\,sr^{-1}} \quad (18)$$

with the total radius R. From Eq. (18) follows the mean surface brightness of the cloud

$$\bar{I}_{[CII]} = \frac{I_{\rm int}}{\pi\,R^2} \ \ \mathrm{erg\,s^{-1}\,cm^{-2}\,sr^{-1}}. \quad (19)$$

To calculate $I_{[CII]}$we assume an exponential temperature profile $T(r) = T_c + T_{\rm surf}E_2(\lambda A_V)$ with the the second order exponential integral E_2, and an arbitrary fitting parameter λ. The central temperature T_c and the parameter λ are different for each

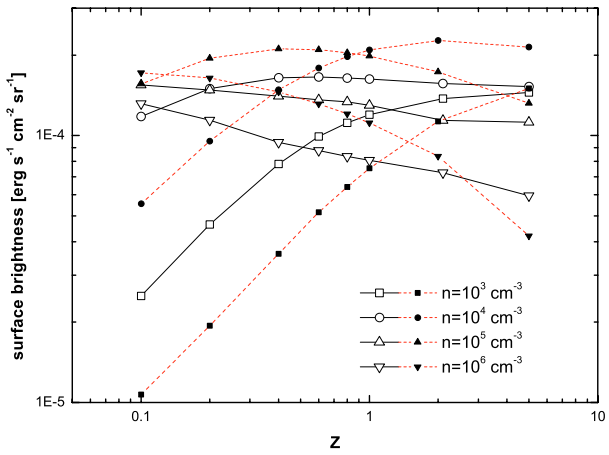

Fig. 5. The surface brightnesses of the [CII] 158 μm (dashed-dotted) emission lines from the KOSMA-τ results (open symbols) and the approximation from Eq. (19) (filled symbols) plotted against the metallicity for different densities. The cloud mass is $M = 10\ M_\odot$, the UV field strength is $\chi = 100$, the assumed central temperature is $T_c = 35$ K, and $\lambda = 4$.

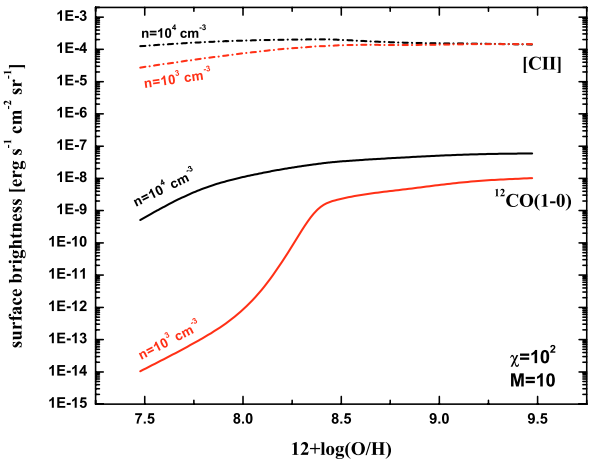

Fig. 6. The surface brightnesses of the [CII] 158 μm (dashed-dotted) and ^{12}CO(1−0) 2.6 mm (solid) emission lines plotted against the metallicity for two different densities. The cloud mass is $M = 10\ M_\odot$ and the UV field strength is $\chi = 100$.

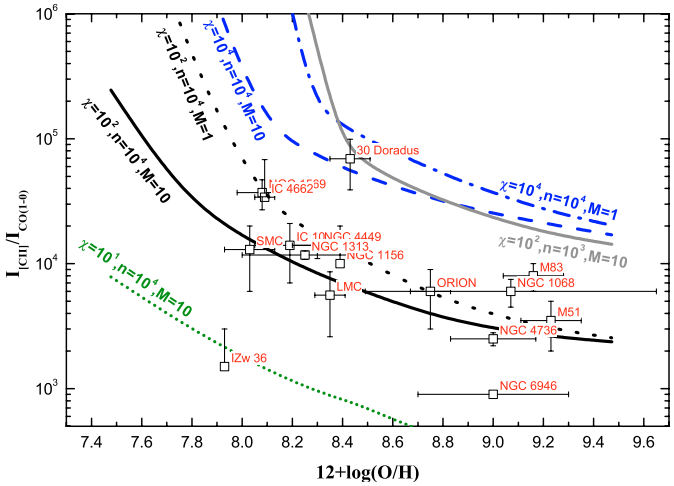

Fig. 7. The intensity ratio $I_{[CII]158\ \mu m}/I_{CO(1-0)}$ is plotted against the metallicity ($Z = 1$ is equivalent to $12 + \log(O/H) = 8.48$). The lines denote the KOSMA-τ results for two different clump masses $M = 1$ and $M = 10\ M_\odot$. The density at the surface of the clumps and the UV field strength in units of the standard Draine field are given in the plot. The observed ratios of nearby galaxies are plotted as squares.

set of PDR parameters. For demonstration purposes we chose $T_c = 35$ K and $\lambda = 4$ to estimate the surface brightnesses for multiple PDRs simultaneously. In Fig. 5 we compare these approximations with the detailed KOSMA-τ results for $I_{[CII]}$. The metallicity dependent behavior is reproduced very well and the quantitative agreement is within a factor of 2 assuming the same temperature profile for all 4 models! If we drop this assumption and use individual temperature profiles for each model the agreement is 10−30%.

Importantly, the total surface brightness does not scale linearly with the surface density of the clouds. Rather it peaks for intermediate values of n, depending on Z. This is mainly a geometrical effect, which can be understood by some qualitative arguments. If we assume that [CII] is optically thin, we see all C^+ atoms. In the low density case, where ionized carbon fills the whole cloud, the surface brightness is then proportional to $n\,(V/A)$, with the volume of the cloud V and the projected area A, hence $\bar{I}_{[CII]} \propto n\,R$. But $R \propto n^{-1/3}$, since we kept the cloud mass constant, and thus we find $\bar{I}_{[CII]} \propto n^{2/3}$. For higher densities the width of the C^+ layer decreases faster than it is compensated by the growing n. The relative thickness of the C^+ layer becomes very small for higher densities (i.e. if $D_{C^+} \ll R$). The surface brightness then is proportional to $n\,4\,\pi\,R^2\,D_{C^+}/(\pi\,R^2)$, hence $\bar{I}_{[CII]} \propto n\,D_{C^+}$. We observe a reduced surface brightness caused by the geometry of the cloud. This is inverse to the common area filling effect for optically thick lines, like e.g. CO (1−0), where the projected area of the CO core decreases with decreasing density as demonstrated in Fig. 5. This was also mentioned by Störzer et al. (1996). This means, that even though the local emissivity $\Lambda_{[CII]}$ scales linearly with n (see Eq. (A.2)), this is not true for the total surface brightness. As a second order effect we also notice a temperature dependence of the local emissivity. The differences between our analytical model and the detailed temperature structures from the PDR calculations are responsible for most of the deviations shown in Fig. 5.

We use our PDR model calculations to study the metallicity dependence of the [CII]/CO(1−0) line ratio. We adopt a density of 10^4 cm^{-3}, a $\gamma = 1.5$, and a UV field, $\chi = 10^2$ similar to the values assumed by Bolatto et al. (1999). Their prediction is an average over a clump ensemble as a model for the large scale emission from the ISM. In contrast, we start here by investigating the metallicity dependence for a single, typical clump. The discussion below shows that this is already sufficient to reproduce the observed trends versus metallicity. The detailed investigation of the effects of averaging over a clump ensemble are left to a subsequent paper. Figure 6 summarizes the results for this typical clump. The dominance of the geometrical effect is reflected in the almost constant [CII] surface brightnesses in Fig. 6. Hence the line ratio [CII]/CO decreases for increasing metallicities and tends to be constant for very high values of Z.

Figure 7 shows that the trend in the observed ratios in normal galaxies can be represented by a single-clump model with $M = 1 \ldots 10^1\ M_\odot$, shown as solid and dotted lines in Fig. 7. We also plotted model results for different cloud parameters to demonstrate how different observations may be explained by different local physical conditions, e.g. the higher observed ratio for the 30 Doradus region can be explained by a similar model, but exposed to an UV field of $\chi = 10^4$ (or alternatively by a clump of less mass). This is consistent with derived FUV strengths for 30 Doradus (Kaufman et al. 1999). The peculiar source IZw 36,

with a very low [CII]/CO ratio at extremely low metallicity can be approximated by a model with a lower FUV field of $\chi \approx 10$, consistent with estimations by Mochizuki et al. (1998).

Our model results for single clumps reproduce qualitatively the results shown by the semi-analytical clumpy model of (Bolatto et al. 1999) for a clump ensemble in reproducing the trends versus metallicity. Thus we can confirm Bolatto's findings whan taking the detailed physical and chemical structure of the clumps into account.

From a practical point of view it is obvious that a clumpy ensemble of different clouds should be closer to the true local conditions than a single spherical clump, but we find that a clumpy approach is not necessary to explain the observerved trend with Z. To model the [CII]/CO line ratio of a particular source in detail it may of course be necessary to apply a clumpy approach. But to understand the general behavior for different metallicities it is sufficient to consider a single, typical clump.

5. Summary

We study the effects of metallicity variations on the gas temperature and [CII] emission line properties of spherical PDRs. We find that the surface temperature of PDRs at high UV fields varies linearly with metallicity. For low UV fields and high densities this metallicity behavior of the surface temperature is converse, showing an inverse dependence with metallicity due to the dominant H_2 heating. We introduce a new two level FUV H_2 heating and cooling function that properly accounts for energy losses via vibrational collisional excitations.

We examine the dependence of the C^+ envelope on metallicity and find that its geometrical depth scales inversely with Z. This produces a higher [CII]/CO($J = 1{-}0$) line ratio at lower metallicities. We used the numerical results from the KOSMA-τ model to study the dependence of PDR emission lines with metallicity. The observed variation of [CII]/CO($J = 1{-}0$) with metallicity can be explained well by a single-clump model and it is not necessary to refere to an average over a clump ensemble. We conclude that the [CII]/CO($J = 1{-}0$) line ratios for sources with differing metallicities do not provide a strong constraint on the clumpy morphology of a molecular clouds.

Acknowledgements. This work is supported by the Deutsche Forschungs Gemeinschaft (DFG) via Grant SFB 494. A.S. thanks the Israel Science Foundation for support. We thank the anonymous referee for her/his helpful comments.

References

Arimoto, N., Sofue, Y., & Tsujimoto, T. 1996, PASJ, 48, 275
Asplund, M., Grevesse, N., Sauval, A. J., Allende Prieto, C., & Kiselman, D. 2004, A&A, 417, 751
Bakes, E. L. O., & Tielens, A. G. G. M. 1994, ApJ, 427, 822
Baumgartner, W. H., & Mushotzky, R. F. 2005, ApJ, submitted
Boger, G. I., & Sternberg, A. 2005, ApJ, 632, 302
Boissé, P. 1990, A&A, 228, 483
Bolatto, A. D., Jackson, J. M., & Ingalls, J. G. 1999, ApJ, 513, 275
Bolatto, A. D., Jackson, J. M., Wilson, C. D., & Moriarty-Schieven, G. 2000, ApJ, 532, 909
Boselli, A., Lequeux, J., & Gavazzi, G. 2002a, A&A, 384, 33
Boselli, A., Gavazzi, G., Lequeux, J., & Pierini, D. 2002b, A&A, 385, 454
Bresolin, F., Garnett, D. R., & Kennicutt, R. C. 2004, ApJ, 615, 228
Burke, J. R., & Hollenbach, D. J. 1983, ApJ, 265, 223
Burton, M. G., Hollenbach, D. J., & Tielens, A. G. G. M. 1990, ApJ, 365, 620
Cazaux, S., & Tielens, A. G. G. M. 2004, ApJ, 604, 222
Cazaux, S., & Spaans, M. 2004, ApJ, 611, 40
Crawford, M. K., Genzel, R., Townes, C. H., & Watson, D. M. 1985, ApJ, 291, 755
d'Hendecourt, L., & Léger, A. 1987, A&A, 180, L9
Draine, B. T. 1978, ApJS, 36, 595
Elmegreen, B. G., & Falgarone, E. 1996, ApJ, 471, 816
Federman, S. R., Sheffer, Y., Lambert, D. L., & Gilliland, R. L. 1993, ApJ, 413, L51
Gierens, K. M., Stutzki, J., & Winnewisser, G. 1992, 259, 271
Giveon, U., Sternberg, A., Lutz, D., Feuchtgruber, H., & Pauldrach, A. W. A. 2002, ApJ, 566, 880
Gorti, U., & Hollenbach, D. 2002, ApJ, 573, 215
Hegmann, M., & Kegel, W. H. 2003, MNRAS, 342, 453
Heydari-Malayeri, M., Melnick, J., & Martin, J.-M. 1990, A&A, 234, 99
Heithausen, A., Bensch, F., Stutzki, J., Falgarone, E., & Panis, J. F. 1998, A&A, 331, L65
Hollenbach, D., & Salpeter, E. E. 1971, ApJ, 163, 155
Hollenbach, D., Werner, M. W., & Salpeter, E. E. 1971, ApJ, 163, 165
Hollenbach, D. J., & Tielens, A. G. G. M. 1997, ARA&A, 35, 179
Hollenbach, D. J., & Tielens, A. G. G. M. 1999, Rev. Mod. Phys, 71, 173
Hollenbach, D., & McKee, C. F. 1979, ApJS, 41, 555
Hollenbach, D. J., Takahashi, T., & Tielens, A. G. G. M. 1991, ApJ, 377, 192
Howe, J. E., Jaffe, D. T., Genzel, R., & Stacey, G. J. 1991, ApJ, 373, 158
Hunter, D. A., Kaufman, M., Hollenbach, D. J., et al. 2001, ApJ, 553, 121
Israel, F. P. 1997, A&A, 328, 471
Israel, F. P., Baas, F., Rudy, R. J., Skillman, E. D., & Woodward, C. E. 2003, A&A, 397, 87I
Kaufman, M. J., Wolfire, M. G., Hollenbach, D. J., & Luhman, M. L. 1999, ApJ, 527, 795
Kobulnicky, H. A., & Skillman, E. D. 1997, ApJ, 489, 636
Köster, B., Störzer, H., Stutzki, J., & Sternberg, A. 1994, A&A, 284, 545
Kramer, C., Stutzki, J., Rohrig, R., & Corneliussen, U. 1998, A&A, 329, 249
Kramer, C., Jakob, H., Mookerjea, B., et al. 2004, A&A, 424, 887
Kramer, C., Mookerjea, B., Bayet, E., et al. 2005, A&A, submitted
Kunth, D., & Östlin, G. 2000, A&ARv, 10, 1K
Le Bourlot, J., Pineau Des Forets, G., Roueff, E., & Flower, D. R. 1993, A&A, 267, 233
Lee, H., Grebel, E. K., & Hodge, P. W. 2003, A&A, 401, 141
Lepp, S., & Dalgarno, A. 1988, ApJ, 335, 769
Lequeux, J., Le Bourlot, J., Des Forets, G. P., et al. 1994, A&A, 292, 371
Li, A., & Draine, B. T. 2002, ApJ, 576, 762
Lisenfeld, U., & Ferrara, A. 1998, ApJ, 496, 145
Lord, S. D., Hollenbach, D. J., Colgan, S. W. J., et al. 1995, ASP Conf. Ser., 73, 151
Luhman, M. L., Satyapal, S., Fischer, J., et al. 2003, ApJ, 594, 758
Madden, S. C. 2000, NewAR, 44, 249
Madden, S. C., Poglitsch, A., Geis, N., Stacey, G. J., & Townes, C. H. 1997, ApJ, 483, 200
Malhotra, S., Hollenbach, D., Helou, G., et al. 2000, ApJ, 543, 634
McKee, C. F. 1989, ApJ, 345, 782
Meixner, M., & Tielens, A. G. G. M. 1993, ApJ, 405, 216
Millar, T. J., Farquhar, P. R. A., & Willacy, K. 1997, A&AS, 121, 139
Mochizuki, K., Onaka, T., & Nakagawa, T. 1998, ASP Conf. Ser., 132, 386
Nikola, T., Geis, N., Herrmann, F., et al. 2001, ApJ, 561, 203
Pak, S., Jaffe, D. T., van Dishoeck, E. F., Johansson, L. E. B., & Booth, R. S. 1998, ApJ, 498, 735
Petitpas, G. R., & Wildosn, C. D. 2003, ApJ, 587, 649
Pierini, D., Leech, K. J., Tuffs, R. J., & Völkl, H. J. 1999, MNRAS, 303, L29
Pierini, D., Leech, K. J., & Völkl, H. J. 2003, A&A, 397, 871
Pustilnik, S. S., Kniazev, A. Y., Musegosa, J., et al. 2002, A&A, 389, 779
Röllig, M., Hegmann, M., & Kegel, W. H. 2002, A&A, 392, 1081
Rubio, M., Boulanger, F., Rantakyro, F., & Contursi, A. 2004, A&A, 425, L1
Simon, R., Stutzki, J., Sternberg, A., & Winnewisser, G. 1997, A&A, 327, L9
Simon, R., Jackson, J. M., Clemens, D. P., Bania, T. M., & Heyer, M. H. 2001, ApJ, 551, 747
Spaans, M. 1996, A&A, 307, 271
Spaans, M., & van Dishoeck, E. F. 1997, A&A, 323, 953
Stacey, G. J., Geis, N., Genzel, R., et al. 1991, ApJ, 373, 423
Steiman-Cameron, T. Y., Haas, M. R., Tielens, A. G. G. M., & Burton, M. G. 1997, ApJ, 478, 261
Sternberg, A. 2004, Proceedings, The dense interstellar medium in galaxies, Proc. of the 4th Cologne-Bonn-Zermatt Symposium, Zermatt, Switzerland, 22–26 September 2003, ed. S. Pfalzner, C. Kramer, C. Staubmeier, & A. Heithausen, Springer proceedings in physics, 91 (Berlin, Heidelberg: Springer)
Sternberg, A., & Dalgarno, A. 1989, ApJ, 338, 197
Sternberg, A., & Dalgarno, A. 1995, ApJS, 99, 565
Störzer, H., Stutzki, J., & Sternberg, A. 1996, A&A, 310, 592
Störzer, H., Zielinsky, M., Stutzki, J., & Sternberg, A. 2000, A&A, 358, 682
Stutzki, J., Stacey, G. J., Genzel, R., et al. 1988, ApJ, 332, 379
Talent, D. L. 1980, BAAS, 12, 866
Thuan, T. X., Sauvage, M., & Madden, S. 1999, ApJ, 516, 783
Tielens, A. G. G. M., & Hollenbach, D. 1985, ApJ, 291, 722
van Dishoeck, E. F. 1988, in Rate Coefficients in Astrochemistry, ed. T. J. Millar, & D. A. Williams (Dordrecht: Kluwer Academic Publishers), 49
Verstrate, L., Léger, A., d'Hendecourt, L., Dutuit, O., & Defourneau, D. 1990, A&A, 237, 436
Warin, S., Benayoun, J. J., & Viala, Y. P. 1996, A&A, 308, 535
Wilson, C. D. 1995, ApJ, 448, L97
Wolfire, M. G., Hollenbach, D., McKee, C. F., Tielens, A. G. G. M., & Bakes, E. L. O. 1995, ApJ, 443, 152
Zaritsky, D., Kennicutt, R. C., Jr., & Huchra, J. P. 1994, ApJ, 420, 87
Zielinsky, M., Stutzki, J., & Störzer, H. 2000, A&A, 358

Online Material

Appendix A: Cooling functions

The cooling of the gas is dominated by fine structure line emission of [CII] and [OI]. The line cooling rate can always be written as $\Lambda_{\rm ul} = n_{\rm u}\, A_{\rm ul}\, E_{\rm ul}\, \beta(\tau_{\rm ul})$ erg s^{-1} cm^{-3} where β is the escape probability, $A_{\rm ul}$ is the transition probability and $n_{\rm u}$ the number of atoms in the upper state u and $E_{\rm ul}$ is the corresponding transition energy (Hollenbach & McKee 1979). Below the critical density for the [OI] emission $n_{\rm cr} = 8.5 \times 10^{-5}\,(100K/T)^{0.69}$ cm^{-3}, the main cooling is provided by the 158 μm [CII] line. The general cooling rate of a two-level system S can be expressed as:

$$\Lambda_{\rm ul} = \frac{n_{\rm S}\, A_{\rm ul}\, E_{\rm ul}\, \beta}{1 + \frac{g_{\rm l}}{g_{\rm u}} \exp(E_{\rm ul}/kT)(1 + \frac{n_{\rm cr}\beta}{n})} \ {\rm erg\,cm^{-3}\,s^{-1}}. \tag{A.1}$$

The critical density for collisional de-excitation $n_{\rm cr} = A_{\rm ul}/\gamma_{\rm ul}$ for the [CII] 158 μm transition is 2.6×10^3 cm^{-3}. The densities we are interested in are in the range of $10^3 ... 10^6$ cm^{-3}. Inserting the numerical values for [CII] and assuming a relative carbon abundance of $1.4 \times 10^{-4} \times Z$ we obtain the cooling rate for the [CII] 158 μm transition:

$$\Lambda_{\rm CII} = \frac{2.02 \times 10^{-24}\, n\, Z}{1 + \frac{1}{2}\exp(92/T)\left(1 + \frac{1300}{n}\right)} \ {\rm erg\,cm^{-3}\,s^{-1}}. \tag{A.2}$$

The general cooling rate of the [OI]63 μm ($^3P_1 \rightarrow {}^3P_2$) and [OI]146 μm ($^3P_0 \rightarrow {}^3P_1$) transitions, only accounting for transitions between neighboring levels, are:

$$\Lambda_{12} = A_{12}\, E_{12}\, \beta\, Z \left(\frac{n_{\rm OI}\, \exp(E_{01}/T)\, g_1\, n\, (n + \beta\, n_{cr,01})}{g_0\, n^2\ \exp(E_{01}/T)\, (n + \beta\, n_{cr,01})\, (g_1\, n\ + \exp(E_{12}/T)\, g_2\, (n + \beta\, n_{cr,12}))} \right) \ {\rm erg\,cm^{-3}\,s^{-1}} \tag{A.3}$$

$$\Lambda_{01} = A_{01}\, E_{01}\, \beta\, Z \left(\frac{n_{\rm OI}\, g_0\, n^2}{g_0\, n^2\ \exp(E_{01}/T)\, (n + \beta\, n_{cr,01})\, (g_1\, n\ + \exp(E_{12}/T)\, g_2\, (n + \beta\, n_{cr,12}))} \right) \ {\rm erg\,cm^{-3}\,s^{-1}}. \tag{A.4}$$

Inserting the numerical values for [OI] and a relative oxygen abundance of $3 \times 10^{-4} \times Z$ in the above equation leads to:

$$\begin{aligned} \Lambda_{63\,\mu{\rm m}} &= 3.15 \times 10^{-14}\, 8.46 \times 10^{-5}\, \frac{1}{2}\, Z \\ &\times \frac{3 \times 10^{-4}\, n\, \exp(98\,{\rm K}/T)\, 3\, n\, \left(n + \frac{1}{2}\frac{1.66\times10^{-5}}{1.35\times10^{-11}\,T^{0.45}}\right)}{n^2\ + \exp(98\,{\rm K}/T)\left(n\ + \frac{1}{2}\frac{1.66\times10^{-5}}{1.35\times10^{-11}\,T^{0.45}}\right)\left(3\,n\ + \exp(228\,{\rm K}/T)\,5\,\left(n\ + \frac{1}{2}\frac{8.46\times10^{-5}}{4.37\times10^{-12}\,T^{0.66}}\right)\right)} \ {\rm erg\,cm^{-3}\,s^{-1}} \end{aligned} \tag{A.5}$$

$$\begin{aligned} \Lambda_{146\,\mu{\rm m}} &= 1.35 \times 10^{-14}\, 1.66 \times 10^{-5}\, \frac{1}{2}\, Z \\ &\times \frac{3 \times 10^{-4}\, n\, n^2}{n^2\ + \exp(98\,{\rm K}/T)\left(n\ + \frac{1}{2}\frac{1.66\times10^{-5}}{1.35\times10^{-11}\,T^{0.45}}\right)\left(3\,n\ + \exp(228\,{\rm K}/T)\,5\,\left(n\ + \frac{1}{2}\frac{8.46\times10^{-5}}{4.37\times10^{-12}\,T^{0.66}}\right)\right)} \ {\rm erg\,cm^{-3}\,s^{-1}}. \end{aligned} \tag{A.6}$$

This leads to the total [OI] cooling rate $\Lambda_{\rm OI} = \Lambda_{63\,\mu{\rm m}} + \Lambda_{146\,\mu{\rm m}}$. In the high density case gas-grain collisional cooling is also contributing to the total cooling of the cloud:

$$\Lambda_{\rm g-g} = 3.5 \times 10^{-34}\, \sqrt{T}\left(T - T_{\rm grain}\right)\, n^2\, Z. \tag{A.7}$$

$T_{\rm grain}$ is the dust temperature as given by Hollenbach et al. (1991). The total cooling rate is the sum of the above individual rates

$$\Lambda_{\rm tot} = \Lambda_{\rm CII} + \Lambda_{\rm OI} + \Lambda_{\rm g-g}. \tag{A.8}$$

Appendix B: The electron density at PDR surfaces

At the surface of a PDR atomic carbon and sulfur are ionized by the impinging, unshielded FUV radiation and atomic hydrogen is ionized by cosmic rays (FUV ionization of H is prevented by the Lyman limit). Electrons from dust are negligible due to the small number density of dust grains. The relative contribution from these electron donors to the total electron density $n_{\rm e}$ is shown in Fig. B.1 for the low (left) and high FUV (right) case. The values are computed with the KOSMA-τ PDR model. The histogram shows the increasing importance of atomic carbon as main electron source with increasing density. Nevertheless the additional contributions of atomic hydrogen and sulfur are not negligible. Even at very high UV fields, $\chi \approx 10^6$, a relevant fraction of the electrons is generated in the additional ionization processes. At gas densities $\sim 10^{5.5}$ cm^{-3} still 16–20% of the electrons stem from the ionization of atomic hydrogen and sulfur. This fraction increases rapidly with decreasing density, with the result that at a number density of $\sim$1000 cm^{-3} only <40% of the electrons are due to ionization of atomic carbon. We present an analytic approximation to the electron density at PDR surfaces which fits the actual behavior quite accurately and which allows an easy interpretation of the metallicity dependence. We assume

$$n_{\rm e} = (X_{\rm C}\ + X_{\rm S})\, n\, Z + n_{\rm H^+} \tag{B.1}$$

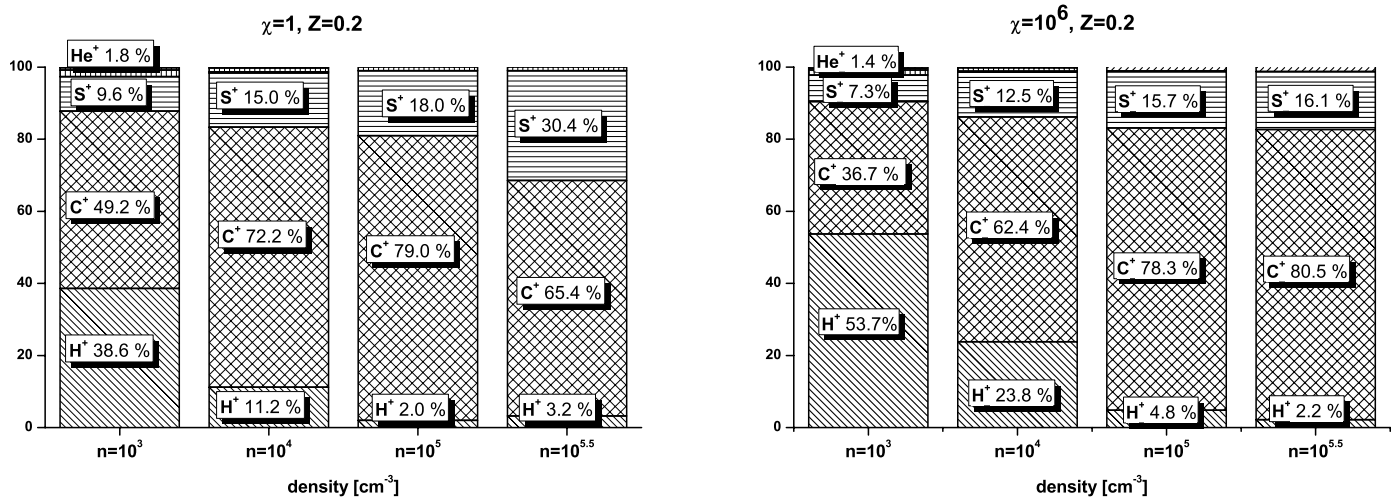

Fig. B.1. The relative contribution of the various electron donors to the total electron density n_e at the cloud surface as computed in the KOSMA-τ model. The percentages are given for different values of surface density n (columns) at FUV fields $\chi = 1$ (*left*) and $\chi = 10^6$ (*right*) and a fixed metallicity of $Z = 0.2$.

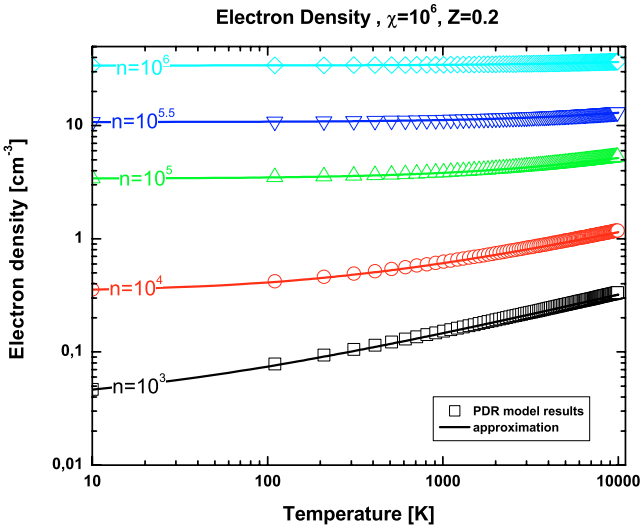

Fig. B.2. A comparison of numerically obtained electron densities (symbols) with the analytical expression (lines) in Eq. (B.4), at $A_V = 0, \chi = 10^6$, $Z = 1$ for different surface densities.

X_C and X_S are the relative elemental abundances of carbon and sulfur ($X_C = 1.4 \times 10^{-4}$, $X_S = 2.8 \times 10^{-5}$, Hollenbach & Tielens 1999; Federman et al. 1993). Together with the balance equation for hydrogen:

$$n_H \zeta = a_H \, n_{H^+} \, n_e, \tag{B.2}$$

where $\zeta = 2.3 \times 10^{-17}$ s^{-1} is the ionization rate due to cosmic rays (Sternberg & Dalgarno 1995), and $a_H = 3.5 \times 10^{-12}(T/300K)^{-0.75}$ s^{-1} is the recombination rate, we get the following expression for the electron density:

$$n_e = \frac{X}{2} n Z \left[1 + \sqrt{1 + \frac{T^{0.75}}{n Z^2} \left(\frac{6.05 \times 10^{-4}}{X} \right)} \right] \quad \mathrm{cm}^{-3} \tag{B.3}$$

with $X = X_C + X_S$. This is in reasonable agreement with the numerical results from the detailed PDR calculations but deviates by 5–10%. The deviations are due to the different net recombination rates when considering all ionized species. To account for this changed rate we have fitted the parameter a in Eq. (B.2) to match the electron density from the full PDR model. Assuming $n_{H^+} \approx C \, n_H \, \zeta / n_e \, a_H$ and fitting the constant C to the numerical values we obtain

$$n_e = \frac{X}{2} n Z \left[1 + \sqrt{1 + \frac{T^{0.75}}{n Z^2} \left(\frac{7.52 \times 10^{-4}}{X} \right)} \right] \quad \mathrm{cm}^{-3}. \tag{B.4}$$

The agreement with the KOSMA-τ results is shown in Fig. B.2. Please note that in the high radiation case all C and S at the surface are ionized so that the ratio of electrons contributed by them directly reflects their abundance ratio.

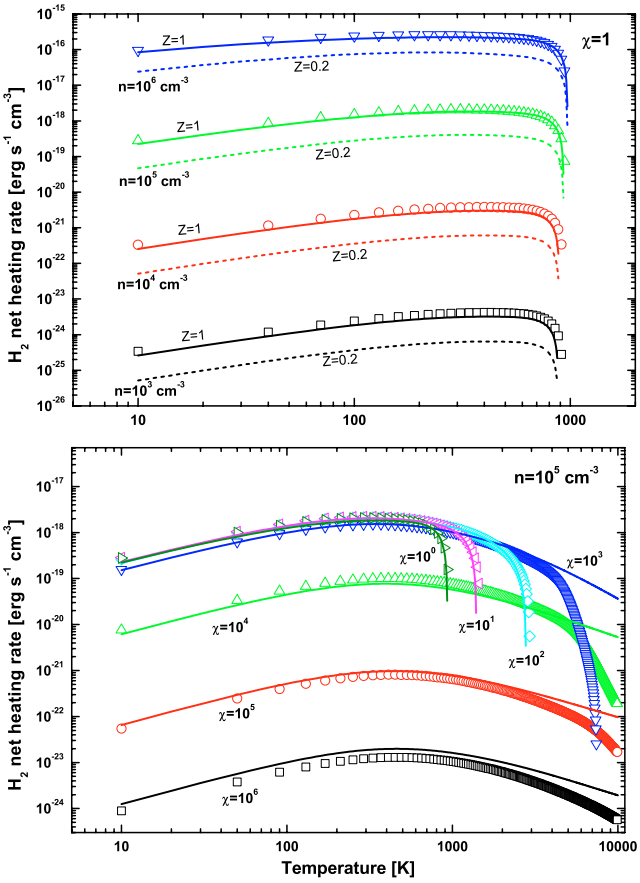

Fig. C.1. The net H_2 heating rate is plotted for different values of surface density n at a $\chi = 1$ FUV field (*top*) and for different UV field strengths for a fixed density of $n = 10^3$ cm^{-3} (*bottom*) over the temperature. The symbols are the numerical results from the 15-level system in the KOSMA-τ model, the curves show the results using our effective two-level approximation. For $\chi = 1$ we also plot a low Z case (solid, $Z = 1$, and dashed, $Z = 0.2$). The deviations at the highest temperatures and radiation fields are due to cooling transitions from higher vibrational levels in this regime which are ignored in our approximation.

Appendix C: H_2 vibrational heating

An important heating processes in dense PDRs is collisional deexcitation of FUV-pumped H_2 molecules (Sternberg & Dalgarno 1995). Here we present a two level approximation for the H_2 vibrational heating and cooling valid in the parameter range where the process plays a major role (see Sect. 2.2.2). The approximation reproduces the net heating rate computed by SD95 assuming transitions among all 15 vibrational levels in the ground electronic state, but neglecting the rotational structure.

Vibrational cooling reduces the net heating at large gas temperatures (see Fig. C.1, bottom). The vibrational cooling is most effective at low χ for which a large H_2 density is maintained. With PDR temperatures of typically less than 2000 K (see Sect. 2) and the energy gap between the two lowest vibrational levels $\Delta E_{0,1} = 5988$ K, we can assume that most of the H_2 is always in the ground ($v = 0$) level in this regime. Vibrational cooling is thus basically given by collisional excitation to $v = 1$ followed by either radiative decay or photodissociation. Using the molecular constants for the lowest vibrational transition we obtain the collisional cooling rate

$$\Lambda_{H_2} = -\Delta E_{1,0}\,\gamma_{1,0}\exp\left(\frac{-\Delta E_{1,0}}{k\,T}\right) n\,n_{H_2}\,\frac{A_{1,0}+\chi\,D_1}{\gamma_{1,0}\,n + A_{1,0} + \chi\,D_1} \tag{C.1}$$

with the spontaneous emission rate coefficient $A_{1,0} = 8.6 \times 10^{-7}$ s^{-1}, the collisional rate coefficient $\gamma_{1,0} = 5.4 \times 10^{-13}\sqrt{T}$ s^{-1} cm^{-3}, and the standard photodissociation rate for the $v = 1$ level of $D_1 = 2.6 \times 10^{-11}$ s^{-1} (Sternberg & Dalgarno 1995). We found that the fit can be improved if $\Delta E_{0,1}$ is increased by 10%.

In contrast vibrational heating is important when the FUV radiation field provides a significant pumping to higher vibrational states. Thus we define a separate equivalent two-level system for the heating. It is characterized by the effective coefficients $\Delta E_{\rm eff}$, $A_{\rm eff}$, $\gamma_{\rm eff}$, and $D_{\rm eff}$ providing the same heating rate as the full 15 level system

$$\Gamma_{H_2^*} = n_{H_2}\sum_j\sum_{i\geq j}\frac{\chi\,P_i\,\Delta E_j}{1+[A_j+\chi\,D_j]/[\gamma_j\,n]} \tag{C.2}$$

$$= n_{H_2}\frac{\chi\,P_{\rm tot}\,\Delta E_{\rm eff}}{1+[A_{\rm eff}+\chi D_{\rm eff}]/[\gamma_{\rm eff}\,n]}. \tag{C.3}$$

The quantity P_i denotes the formation rate of vibrationally excited H_2 for the different levels, $P_{\rm tot}$ represents the sum rate over all levels. The effective coefficients can be easily obtained by considering different asymptotic values of the density n and the radiation field χ. This yields $P_{\rm tot} \cdot \Delta E_{\rm eff} = 9.4 \times 10^{-22}$ erg s^{-1}, $\gamma_{\rm eff} = \gamma_{1,0}, D_{\rm eff} = 4.7 \times 10^{-10}$ s^{-1}, and $A_{\rm eff} = 1.9 \times 10^{-6}$ s^{-1}. A comparison of the heating rates using our effective two-level system with the results using the 15-level molecule in our KOSMA-τ model is shown in Fig. C.1. Here, we scan the parameter ranges where the H_2 vibrational heating and cooling gives a major contribution to the overall energy balance (see Fig. 2). In the upper plot representing low radiation fields and varying densities we find an almost perfect agreement of the two level approximation with the full numeric treatment. At high densities and varying radiation fields shown in the lower plot, we find a good match at temperatures below about 3000 K. The deviation at higher temperatures is due to the neglect of cooling contributions from higher vibrational levels. It has no impact on the overall PDR model, because photoelectric heating clearly supersedes the vibrational contribution at these conditions.

With the simple analytic two-level approximation, we can easily understand the quantitative behavior of the H_2 vibrational energy balance from basic principles thus providing a handy tool for estimates of temperature structures. Burton et al. (1990) also introduced a two-level approximation for the H_2 heating. However, they considered only a single pseudo excited level with an energy corresponding to $v = 6$ and hence did not properly account for cooling via rapid excitation to $v = 1$, or heating via pumping and collisional deexcitation from all 15 levels.